IMPROVED PHOTOCATALYTIC PROPERTIES OF FLOWER-LIKE $Bi_2O_2CO_3/TiO_2$ NANOCOMPOSITE STRUCTURES

Y. LIAN[b], L. YING[a], C. LI[c], H. WANG[a*]
[a]*College of Biological, Chemical Sciences and Engineering, Jiaxing University, Jiaxing, Zhejiang 314001, China*
[b]*College of Material and Textile Engineering, Jiaxing University, Jiaxing, Zhejiang 314001, China*
[c]*Department of Physics and Key Laboratory of Artificial Micro- and Nano-structures of Ministry of Education, Wuhan University, Wuhan 430072, China*

In this paper, hierarchical composites of TiO_2 nanoparticles supported on flower-like spherical $Bi_2O_2CO_3$ structures were synthesized by a two-step hydrothermal method. The prepared samples were characterized using X-ray diffraction (XRD), scanning electron microscope (SEM), X-ray photoelectron spectroscopy (XPS), UV-Vis diffuse reflectance spectrometry (DRS), photoluminescence (PL) and photocurrent measurement. The photocatalytic activity of the composites was investigated as a function of the amount of TiO_2 in the degradation of RhB under UV-Vis light irradiation. The $Bi_2O_2CO_3/TiO_2$ composites exhibited significantly enhanced performance compared with pure $Bi_2O_2CO_3$ or TiO_2. For instance, the $Bi_2O_2CO_3/TiO_2$ composite with 0.44 mL tetrabutyl titanate addition (*i.e.* BT-2) showed the best photocatalytic activity, which is about 3.7 times and 4.3 times as high as that of pure TiO_2 or $Bi_2O_2CO_3$, respectively. The improved performance of the $Bi_2O_2CO_3/TiO_2$ composites can be attributed to the formation of binary heterojunctions, which facilitate separation of photogenerated electron-hole pairs. Furthermore, the composites showed high stability and long-term reusability. To better understand the photocatalytic mechanism, experiments involving active species trapping were conducted, revealing that the holes and hydroxyl radicals played key roles in the photocatalytic reaction process.

(Received August 2, 2017; Accepted November 15, 2017)

Keywords: $Bi_2O_2CO_3/TiO_2$ composites; Binary heterojunction; Photocatalytic degradation

1. Introduction

Photocatalysis is a promising for environmental applications in areas such as degradation of organic pollutants, production of H_2 by water splitting, treatment of polymers and biological materials [1-6]. TiO_2 is the most widely studied photocatalyst due to its high photoactivity, chemical stability and low cost [7]. However, its wide bandgap of 3.2 eV limits its absorption to the UV region with essentially no absorption in the visible. Also, due to a high density of bandgap states, its photogenerated electrons and holes recombine quickly via non-radiative pathways, resulting in low overall photocatalytic activity [8]. It is therefore of strong interest to develop strategies to enhance visible absorption and/or reduce electron-hole recombination in TiO_2. One such strategy is to use heterojunctions involving TiO_2 that can not only narrow its bandgap but also effectively reduce photoinduced electron-hole recombination [9, 10].

In the meantime, inspired by the highly efficient natural photosynthesis based on plants leaves that are pseudo two-dimensional (2D) structures, there have been strong interest in developing 2D nanomaterials for photocatalysis applications. One example is 2D bismuth subcarbonate ($Bi_2O_2CO_3$) nanomaterials that have attracted increasing attention recently [11]. In

*Corresponding author: hongmei256@163.com

particular, $Bi_2O_2CO_3$ with a Sillen layered structure has recently been studied as a photocatatalyst. For example, Xie *et al*. synthesized [001] facet exposed flower-like $Bi_2O_2CO_3$ hierarchitecture and the resulting material showed enhanced photocatalytic activity under the solar light [12]. Similarly, $Bi_2O_2CO_3$ hollow microspheres prepared by a template-free hydrothermal method were used in photocatalytic removal of indoor NO, which was more effective than P25, C-doped TiO_2, and $Bi_2O_2CO_3$ particles [13]. Flower-like $Bi_2O_2CO_3$ microspheres prepared by a hydrothermal method exhibited higher activity than P25 for the photocatalytic degradation of Rhodamine B (RhB) while $Bi_2O_2CO_3$ plates showed lower activity than P25 [14]. It has been found that the bandgap of $Bi_2O_2CO_3$ is dependent on its structure and morphology that in turn are affected by preparation method. For instance, the bandgap of the flower-like $Bi_2O_2CO_3$ hierarchitecture synthesized by Xie *et al*. is 3.1 eV [12], whereas the $Bi_2O_2CO_3$ microspheres reported by Madhusudan *et al*. showed an indirect bandgap of 2.25 eV and a direct bandgap of 3.3 eV, respectively [14].

In this work, we have synthesized $Bi_2O_2CO_3/TiO_2$ composite photocatalyst that shows enhanced absorption in the visible light due to $Bi_2O_2CO_3$ and suppressed electron-hole recombination due to the heterojunction between $Bi_2O_2CO_3$ and TiO_2. This scheme results in overall enhanced photocatalytic activity as demonstrated in the photodegradation study of RhB under simulated sunlight (320 nm < λ < 780 nm) irradiation. The structure and optical properties of the composite photocatalyst was characterized using combination of experimental techniques. A possible photocatalytic mechanism is proposed to account for the observed photocatalytic reactivity.

2. Experiments

2.1 Raw materials

All chemicals (bismuthnitrate pentahydrate, sodium citrate, urea, polyethylene glycol-6000 (PEG-6000), absolute ethanol, tetrabutyl titanate ($C_{16}H_{36}O_4Ti$), benzoquinone, terbutyl alcohol, triethanolamine (TEOA) obtained from Sinopharm Chemical Reagent Co. Ltd were of analytical grade and used as-received without further purification.

2.2 Synthesis of $Bi_2O_2CO_3$

Flower-like $Bi_2O_2CO_3$ were prepared by a typical hydrothermal synthesis with small modifications [15]. First, 0.97 g $Bi(NO_3)_3{\cdot}5H_2O$ was first dissolved into 60 mL deionized water with magnetic stirring. Then, 1.76 g $Na_3C_6H_5O_7$, 0.48 g $CO(NH_2)_2$ and 1 g PEG-6000 were added to the above solution. Next, the mixed solution was stirred continuously for another 1 h. Subsequently, the mixture was transferred into a Teflon-lined stainless steel autoclave with a capacity of 100 mL and heated at 180°C for 12 h. After being cooled down to room temperature naturally, the precipitates were separated from the solution by centrifugation at 3500 rpm for 3 min. Finally, the precipitates were respectively washed with deionized water and absolute ethanol for three times and dried at 70 ^{o}C for several hours.

2.3 Synthesis of $Bi_2O_2CO_3/TiO_2$ composites

$C_{16}H_{36}O_4Ti$ (0.22, 0.44, 0.66 and 0.88 mL) was dissolved into 10 mL absolute ethanol to form solution A. 0.2 g $Bi_2O_2CO_3$ was dispersed into 20 mL absolute ethanol with stirring for 30 min at room temperature to form homogeneous solution B. Next, solution A was added to solution B drop by drop under constant stirring. After stirring for 1 h, the resulting suspension was transferred into a 50 mL Teflon-lined stainless steel autoclave. The mixture was then heated to 180 ^{o}C and maintained for 4 h. Subsequently, the autoclave was cooled to room temperature naturally. The obtained samples were filtered, washed with absolute ethanol and deionized water, and dried at 70 ^{o}C. The products were loaded with varied increasing amount of TiO_2 and named as BT-1, BT-2, BT-3 and BT-4, respectively.

2.4 Characterization of the as-prepared samples

The morphologies of the samples were analyzed by scanning electron microscopy (SEM, Hitachi S-4800) with an accelerating voltage of 10 kV. The crystal structure and crystallinity of the prepared samples were determined using X-ray diffraction (XRD, Bruker D8 Advance diffractometer) with Cu Kα radiation (λ = 1.5406 Å) in the range of 2θ between 10° and 80°, the working voltage with 40 kV and current with 40 mA. The diffuse reflectance spectra (DRS) of the obtained samples were carried on a Shimadzu-UV-2550 equipped with $BaSO_4$ as a reference material. Photoluminescence (PL) spectra were measured using a Hitachi-4600 Fluorescence spectrometer with the excitation wavelength of 300 nm at room temperature. The sample was pressed into a thin disk and fixed on a quartz cell. The chemical states of samples were determined using an X-ray photoelectron spectrum (XPS, Thermo 163 Fisher ESCALAB 250Xi system). The binding energies were normalized using C1*s* peak at 284.6 eV. The photocurrent tests were performed using electrochemical workingstation (CHI660C, Chen hua, China) equipped with an electrochemical cell consisting of saturation calomel as the reference electrode and a platinum mesh as the counter electrode. The prepared thin film was used as the working electrode. Solar simulator with 300 W Xe lamp served as a light source, and 0.5 M Na_2SO_4 solution was used as the electrolyte. The working electrodes were prepared by a dip coating method: 1 mg of photocatalyst was suspended in 1 mL ethanol water and then ultrasonicated for 2 h to make a slurry; the slurry was then dip-coated onto a an indium-tin oxide (ITO) glass substrate (1cm × 2 cm). The electrodes were dried in stove at 50 ^{o}C for 5 h under dark condition.

2.5 Photocatalytic activity measurement

Photocatalytic activities of as-prepared catalysts were evaluated by monitoring the degradation of RhB with a 300 W Xe lamp. Photocatalytic activity of pure $Bi_2O_2CO_3$ and TiO_2 were also measured for comparison. Typically, 20 mg photocatalysts were dispersed in 50 mL RhB solution (10 mg•L^{-1}). Prior to light irradiation, the aqueous suspension was stirred in the dark for 30 min to ensure the establishment of adsorption-desorption equilibrium. After light irradiation, 2 mL of solution was collected every 15 min and immediately centrifuged, the concentration of RhB was determined by measuring its absorption at 554 nm. The whole degradation process was monitored for 90 min. A calibration based on Beer-Lambert Law was used to quantify the concentration.

2.6 Active species trapping experiments

For detecting the active species generated in the photocatalytic reaction, superoxide radical (•O_2^-), holes (h^+) and hydroxyl radicals (•OH) were investigated by adding 1.0 mM benzoquinone (BQ, a scavenger of •O_2^-), triethanolamine (TEOA, a scavenger of h^+), terbutyl alcohol (TBA, a scavenger of •OH), respectively [16]. The method was similar to the former photocatalytic experiments.

3. Results and discussion

3.1 Morphology

The SEM images, as shown in Fig. 1, show the size and morphology of the different photocatalyst samples. Fig.1a for pure $Bi_2O_2CO_3$ reveals flower-like structures with an average diameter of about 1.5 μm. The hierarchical superstructures are composed of many thin nanoplates with thickness of approximately 10 nm. Many petal-like structures on the edges of the $Bi_2O_2CO_3$ flowers can be clearly observed, which may expose large active sites. It can be deduced that during the hydrothermal process, the surfactant PEG could have served as a template to make the $Bi_2O_2CO_3$ nanoplates ultimately form the three-dimensional (3D) hierarchical structure. The SEM images of $Bi_2O_2CO_3/TiO_2$ hybrids are displayed from Fig.1b to e. Fig. 1b and 1c show that TiO_2 nanoparticles with small size decorate the petal-like surface of the $Bi_2O_2CO_3$ nanoplates homogeneously, and the size and morphology of the $Bi_2O_2CO_3$ flowers are well preserved. Apart

from TiO_2 on the surface of $Bi_2O_2CO_3$, no isolated TiO_2 nanoparticles can be found, indicating strong adhesion between TiO_2 nanoparticles and $Bi_2O_2CO_3$. The presence of TiO_2 is hoped to effectively reduce the fast recombination of photogenerated charge carries and thereby enhance photocatalytic activity. Under hydrothermal condition, the interconnection between TiO_2 and $Bi_2O_2CO_3$ is reinforced, forming $Bi_2O_2CO_3/TiO_2$ binary heterostructures. With the increasing amount of tetrabutyl titanate, the flower-like structures of $Bi_2O_2CO_3$ begin to blur and only some $Bi_2O_2CO_3$ petals still could be seen because the surface of the flowers are occupied by a large number of TiO_2 nanoparticles (shown from 1d). When the volume of tetrabutyl titanate reached 0.88 mL, the $Bi_2O_2CO_3$ petals were completely covered by a great number of TiO_2 nanoparticles and the hierarchical structures of flower-like $Bi_2O_2CO_3$ turned into spherical structures (Fig. 1e).

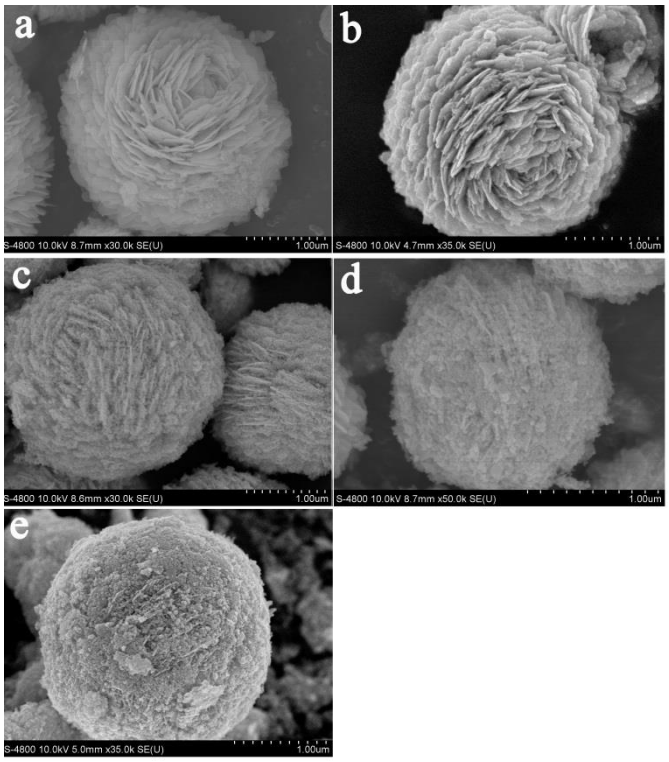

Fig.1 SEM images of pure $Bi_2O_2CO_3$ (a); $Bi_2O_2CO_3/TiO_2$ composite of BT-1 (b); BT-2 (c); BT-3 (d) and BT-4 (e).

3.2 XRD and XPS analysis

The XRD patterns of the pure TiO_2, pure $Bi_2O_2CO_3$, and $Bi_2O_2CO_3/TiO_2$ composites with different loading amount of TiO_2 are shown in Fig. 2. For pure TiO_2 and pure $Bi_2O_2CO_3$, the products are well crystallized and all the distinctive peaks can be indexed to the crystalline structure of anatase TiO_2 (JCPDS, No. 21-1272) [17] and tetragonal $Bi_2O_2CO_3$ (JCPDS 41-1488) [18]. As for the $Bi_2O_2CO_3/TiO_2$ composites, only a small peak appeared at 25.4^o, corresponding to the (101) crystal plane of anatase TiO_2. The result is attributed to the low content of TiO_2 in the composites. In addition, the position and shape of $Bi_2O_2CO_3$ distinctive peaks hardly changed, indicating the incorporation of TiO_2 did not alter the lattice structure of $Bi_2O_2CO_3$, which may be beneficial to photocatalysis based on $Bi_2O_2CO_3/TiO_2$ heterostructures.

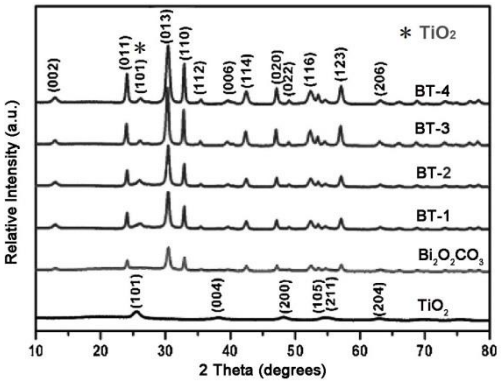

Fig. 2 XRD patterns of TiO_2, $Bi_2O_2CO_3$, BT-1, BT-2, BT-3 and BT-4.

To investigate the surface composition and chemical state of the BT-2 composite, XPS spectra were measured and shown in Fig. 3. All binding energies obtained in the XPS analysis are corrected by referencing C 1*s* at 284.6 eV. Fig. 3a illustrates the full spectrum of $Bi_2O_2CO_3/TiO_2$ in a wide energy range, while Figs. 3b-f focus on the specific binding energies of elements Bi, Ti, C and O, respectively. The Bi 4*f* peaks located at the binding energies of 158.2 eV and 163.4 eV are attributed to Bi $4f_{7/2}$ and Bi $4f_{5/2}$ of Bi^{3+} in accordance with literature [18]. The XPS signals of Ti 2*p* are observed at the binding energies of 458.1 eV (Ti $2p_{3/2}$) and 464.2 eV (Ti $2p_{1/2}$), which correspond to Ti^{4+} [19]. The binding energy of O 1*s* is 530.1 eV, slightly higher than that of pure TiO_2 529.9 eV, which can be attributed to interaction of TiO_2 with $Bi_2O_2CO_3$ [20]. The results of XRD and XPS verify the existence of anatase TiO_2, which are in good accordance with the results of SEM.

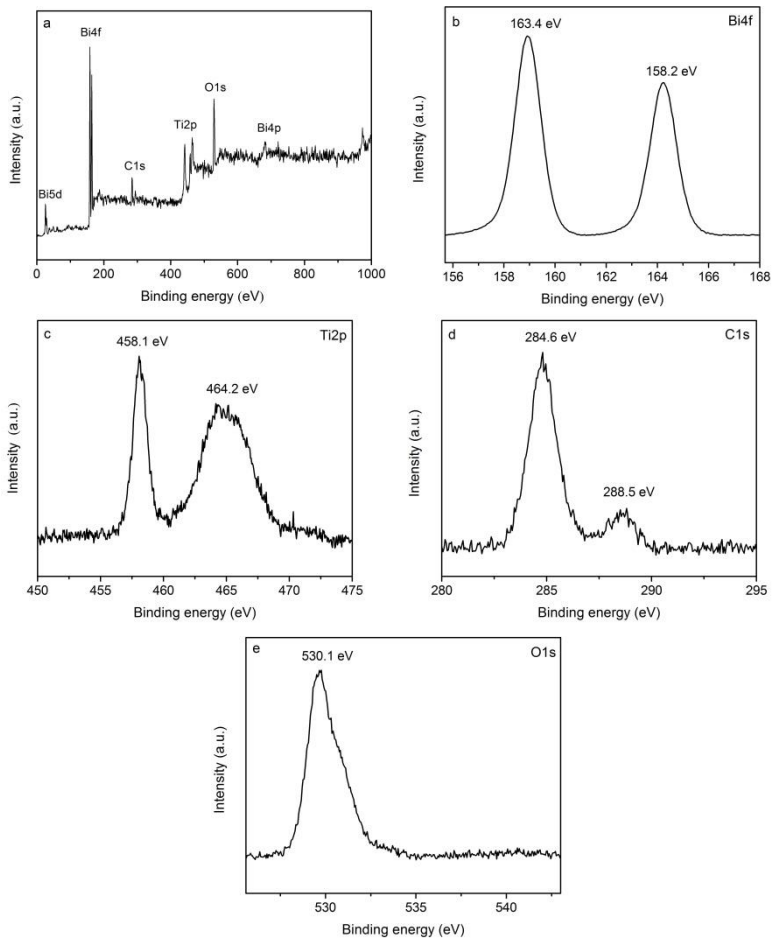

Fig. 3 XPS spectra of BT-2 composites: (a) survey scan; (b) Bi 4f; (c) Ti 2p; (d) C 1s; (e) O 1s.

3.3 Optical absorption and charge separation

The optical properties of pure $Bi_2O_2CO_3$, pure TiO_2 and $Bi_2O_2CO_3/TiO_2$ composites are investigated by the DRS. The extinction spectrum measured consists of both absorption and scattering. While there are some scattering based on the background in the spectrum and expected based on the large size of the sample structures, absorption is expected to be dominant still. As shown in Fig. 4, all the $Bi_2O_2CO_3/TiO_2$ samples show similar spectral features as the pure $Bi_2O_2CO_3$. However, $Bi_2O_2CO_3/TiO_2$ composites have higher extinction intensity than pure $Bi_2O_2CO_3$ both in the UV and visible light region. The extinction intensity of $Bi_2O_2CO_3/TiO_2$ is higher in the UV region than that of pure $Bi_2O_2CO_3$, which can be attributed to absorption of TiO_2. One may anticipate that the composite structures show better photocatalytic activity due to stronger absorption of light in both the UV and visible.

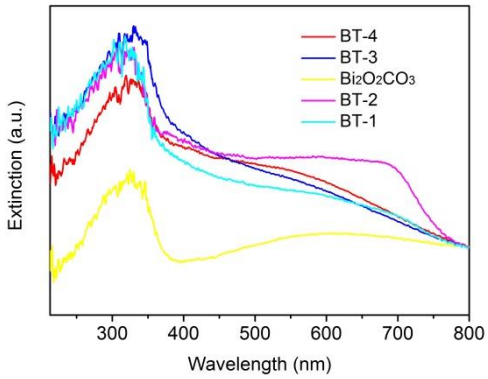

Fig. 4 UV-vis diffuse reflectance spectra of as-prepared samples.

Electron-hole recombination rate has intimate relationship with the photocatalytic activity. The lower the electron-hole recombination rate is, the better photocatalytic activity will be obtained [20]. The PL spectrum can reflect the fate and transfer of photo-induced charge carriers, which are generally one of the key determining factors for the photocatalytic activity. The PL spectra of prepared samples are shown in Fig. 5, which is used to study the electron-hole recombination rate of the as-prepared samples. The pure $Bi_2O_2CO_3$ and TiO_2 emerge strong emission peaks with an excitation wavelength of 300 nm because of the rapid charge recombination. When loading TiO_2 on the $Bi_2O_2CO_3$, the intensity of the emission begins to decrease, which illustrates the recombination rate of electron-hole decreases further. The decreasing electron-hole recombination rate can be attributed to the formation of multiple binary heterojunctions.

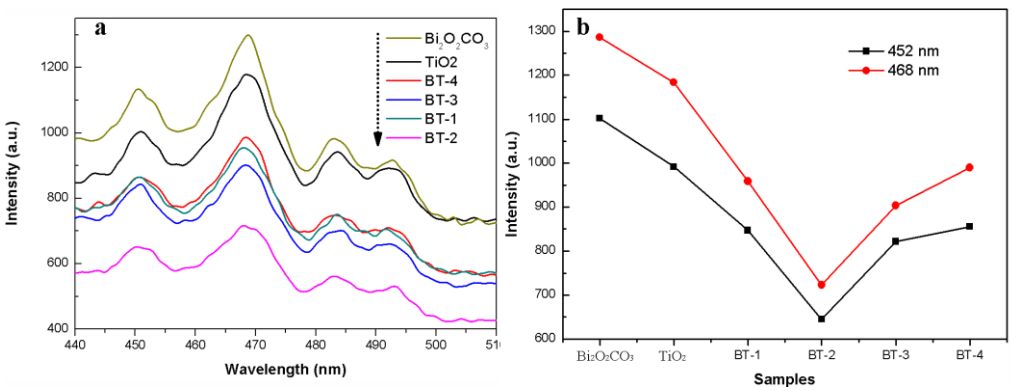

Fig. 5 (a) Room-temperature PL spectra of as-prepared samples; (b) PL intensity at 452 nm and 468 nm for different samples

From Fig. 5, it is also found that the amount of TiO_2 should be adjusted to obtain the best charge separation rate. Firstly, the PL peaks are weakened with increased loading amount of TiO_2 from pure $Bi_2O_2CO_3$ to BT-1, As for the BT-2, the PL intensity is the lowest, which means its photo-generated electron-hole pairs separation efficiency is the highest. That is ascribed to the fact that the electrons are excited from the valence band (VB) to the conduction band (CB) in TiO_2 and then migrate to $Bi_2O_2CO_3$ sheet meanwhile its holes can effectively transfer to the VB of TiO_2, which prevent the direct recombination of electrons and holes. However, with the loading proportion further increasing, the PL intensity returns to normal gradually from BT-3 to BT-4 in the visible light region. This could be because many TiO_2 particles aggregate together in BT-3 and BT-4 (as shown in Fig. 2c), which reduces the contact between TiO_2 and $Bi_2O_2CO_3$. In this case, the formation of heterojunctions between two semiconductors is insufficient, thus the charge separation is not so effective.

3.4 Photocurrent measurements

To investigate the photoelectric properties of the prepared samples, photocurrent measurements were conducted. Fig. 6 shows the photocurrent densities of different electrodes fabricated from TiO_2, $Bi_2O_2CO_3$, BT-1, BT-2, BT-3 and BT-4. When the light is switched on and off, the $Bi_2O_2CO_3/TiO_2$ samples obtain fast reversible enhanced photocurrent response under UV-Vis light irradiation. The photocurrent density of BT-2 (5.2 μA/cm^2) is about 4.3 and 7.4 times than that of pure TiO_2 (1.2 μA/cm^2) or $Bi_2O_2CO_3$ (0.7 μA/cm^2), respectively, suppressed recombination rate of the photoinduced electrons and holes in the binary heterojunction structures.

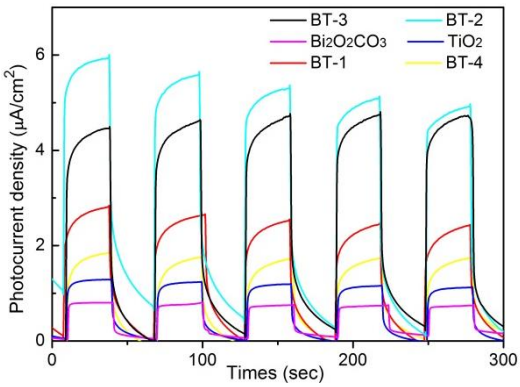

Fig. 6 Photocurrent densities of as-prepared samples

3.5 Photocatalytic performance

The photocatalytic degradation of RhB was performed under simulated sunlight (320 nm < λ < 780 nm) irradiation to study the photocatalytic performance of the synthesized catalysts. Fig. 7a gives the variation of RhB concentration (C/C_0) with the photodegradation time over different photocatalysts. All the $Bi_2O_2CO_3/TiO_2$ composites exhibit higher activity than that of pure TiO_2 and $Bi_2O_2CO_3$. With the increasing of TiO_2 content, the photocatalytic activity is enhanced at first and then decreased with the order of BT-2 > BT-3 > BT-1 > BT-4. The BT-2 photocatalyst shows the best performance and the RhB is decomposed completely after 90 min irradiation. According to the Langmuir-Hinshelwood (L-H) kinetic model, the apparent pseudo-first-order rate constant (min^{-1}) of the photocatalysts are calculated as shown in Fig. 7b. Under light irradiation, reaction rate k of RhB is 0.014 min^{-1} and 0.012 min^{-1} in the presence of TiO_2 and $Bi_2O_2CO_3$, respectively. BT-2 photocatalyst shows the highest activity (k = 0.052 min^{-1}), with a reaction rate 3.7 times and 4.3 times higher than pure TiO_2 or $Bi_2O_2CO_3$, respectively. These results indicates that the heterostructures are much more beneficial to promote effective charges transfer and prolong recombination time of electron-hole pairs [21, 22]. As for $Bi_2O_2CO_3/TiO_2$ composites, the degradation rate firstly increases and then decreases with the increase of loading TiO_2. It is

because that superfluous TiO_2 nanoparticles may lead to agglomeration and be unable to connect with $Bi_2O_2CO_3$ to form heterojunctions [16].

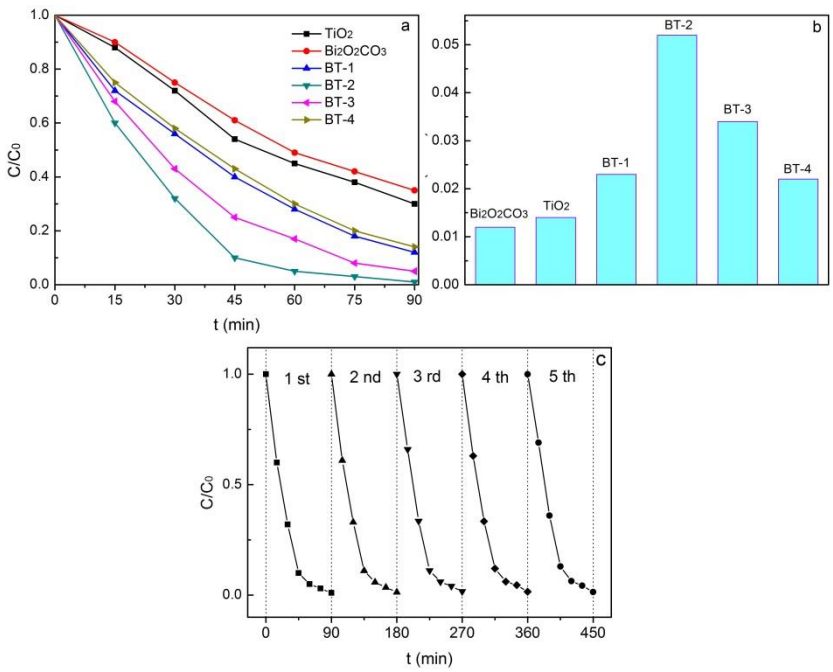

Fig. 7 (a) Change of RhB concentration; (b) the calculated reaction rate under UV-vis light; (c) cycling runs in the degradation of RhB in the presence of BT-2.

The above-mentioned results demonstrated that the degradation process of RhB by BT-2 composite is fast and complete, revealing the excellent photocatalytic activity under UV-vis light irradiation. To evaluate the stability and reusability of BT-2, the cycling runs in the photocatalytic degradation of RhB were done. The photocatalysts would be separated by centrifuging and washing with distilled water to remove the ions absorbed on its surface after every reaction. It can be seen from Fig. 7c that there is no significant decrease of the photocatalytic activity of BT-2 after five cycles. Therefore, these results indicate that the BT-2 composite exhibits high photostability, reusability, and less photocorrosion during the photocatalytic reaction, which have good potential in industrial utilization.

3.6 Possible degradation mechanism

Trapping experiments for detecting active species were conducted during the photocatalytic reaction in the presence of BT-2 composites to help explain the photocatalytic mechanism. As shown in Fig. 8, the degradation efficiency of RhB is not affected by the addition of 1 mM BQ (a scavenger of $\bullet O_2^-$), but apparently decreased with the addition 1 mM TBA (a scavenger of •OH) and 1mM TEOA (a scavenger of h^+). Therefore, the results show that •OH and h^+ are the two primary active species which play key roles in the degradation of RhB rather than $\bullet O_2^-$.

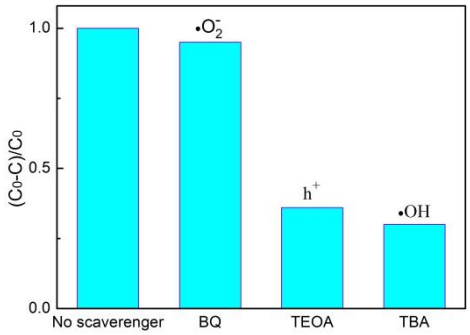

Fig. 8 Effect of scavengers on the photocatalytic degradation of RB by BT-2 composite under UV-vis light irradiation.

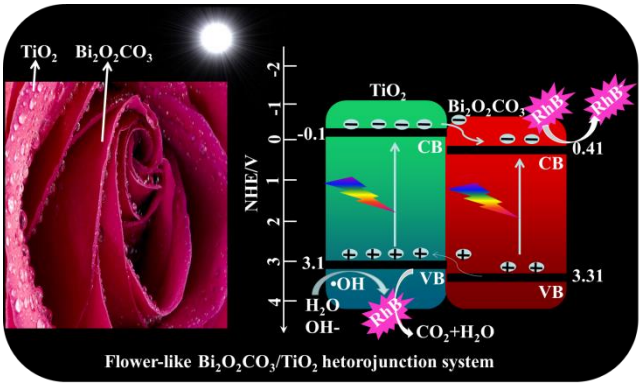

Scheme 1. The mechanism of the photocatalytic RhB degradation and possible band structure of flower-like $Bi_2O_2CO_3/TiO_2$ photocatalyst under UV-vis light irradiation

Based on all the experimental observations, we propose a possible mechanism for the photocatalytic degradation of RhB using BT-2 photocatalyst, as illustrated in Scheme 1. Under UV-Vis light illumination, TiO_2 and $Bi_2O_2CO_3$ can be effectively excited to generate electrons and holes (Eq. (1) and (2)).

$$TiO_2 + h\nu \rightarrow TiO_2(e^-) + TiO_2(h^+) \quad (1)$$

$$Bi_2O_2CO_3 + h\nu \rightarrow Bi_2O_2CO_3(e^-) + Bi_2O_2CO_3(h^+) \quad (2)$$

A local electric field formed for the reason of the conduction band of $Bi_2O_2CO_3$ is more positive than that of TiO_2 nanoparticles. Then the photogenerated electrons in the conduction band of TiO_2 nanoparticles could transfer to that of $Bi_2O_2CO_3$ conduction band, whereas the photogenerated holes in the valence band from the $Bi_2O_2CO_3$ accumulate in the valence band of TiO_2 to form holes center (Eq. (3)). Consequently, the recombination process of electron-hole pairs can be obstructed effectively.

$$Bi_2O_2CO_3(e^- + h^+) + TiO_2(e^- + h^+) \rightarrow Bi_2O_2CO_3(e^-) + TiO_2(h^+) \quad (3)$$

Since the VB potential of TiO_2 is larger than the standard reduction potential of •OH/H_2O and •OH/OH^- [23], the holes on TiO_2 are energetic enough to oxidize H_2O or OH^-, generating •OH (Eq. (4) and (5)), which can react with RhB molecules to produce CO_2 and H_2O.

$$h^+(TiO_2) + H_2O \rightarrow \bullet OH + H^+ \quad (4)$$

$$h^+(TiO_2) + OH^- \rightarrow \bullet OH \quad (5)$$

While the electrons on $Bi_2O_2CO_3$ were unable to reduce O_2 and produce $\bullet O_2^-$ because the CB potential of $Bi_2O_2CO_3$ is lower than the standard redox potential of $O_2/\bullet O^{2-}$ [24]. Nevertheless, these electrons still could reduce pollutant, which is in favor of the photocatalysis enhancement (Eq.(6)).

$$e^-(Bi_2O_2CO_3) + \text{Pollutant} \rightarrow \text{Pollutant}^- \quad (6)$$

Thus, efficient transfer of charges in the above processes contributes to the increase lifetime of the charge carriers and enhances photocatalytic activity and stability.

4. Conclusions

In summary, $Bi_2O_2CO_3/TiO_2$ composites have been successfully fabricated by a facile two-step hydrothermal method. Compared to pure TiO_2 and $Bi_2O_2CO_3$, $Bi_2O_2CO_3/TiO_2$ composites presented the enhanced photocatalytic activity and photochemical stability, and higher efficiency of charge separation. TiO_2 and $Bi_2O_2CO_3$ demonstrate a beneficial synergetic effect for the improvement of photocatalytic performance. The current work provides a new avenue that can improve the UV-Vis light response of TiO_2 and $Bi_2O_2CO_3$, which can expand their application in photocatalytic degradation of organic pollutants in water.

Ackonwledgements

This work was financially supported by the Program for Science and Technology of Zhejiang Province (No. 2017C37030). Besides, we also appreciate the support of the college students' Challenge Cup program.

References

[1] I. Oller, S. Malato, J. A. Sánchez-Pérez, Science of the Total Environment **409**(20), 4141 (2011).
[2] S. Y. Lu, D. Wu, Q. L. Wang, J. Yan, A. G. Buekens, K. F. Cen, Chemosphere **82**(9), 1215 (2011).
[3] A. Kudo, Y. Miseki, Chemical Society Reviews **38**(1), 253 (2009).
[4] H. Hidaka, Y. Suzuki, K. Nohara, S. Horikoshi, Y. Hisamatsu, E. Pelizzetti, N. Serpone Journal of Polymer Science Part A: Polymer Chemistry **34**(7), 1311 (1996).
[5] C. Pulgarin, J. Kiwi, V. Nadtochenko, Applied Catalysis B: Environmental **128**, 179 (2012).
[6] S. Obregón Alfaro, A. Martínez-de la Cruz, Leticia M. Torres-Martínez, S.W. Lee, Catalysis Communications **11**(5), 326 (2010).

[7] A. Fujishima, X. Zhang, D. A. Tryk, Surface Science Reports **63**(12), 515 (2008).
[8] D. T. Zhou, Z. Chen, Q. Yang, X. P. Dong, J. J. Zhang, L. S. Qin, Solar Energy Materials & Solar Cells **157**, 399 (2016).
[9] S. Shenawi-Khalil, V. Uvarov, S. Fronton, I. Popov, Y. Sasson, Applied Catalysis B: Environmental **117-118**, 148 (2012).
[10] F. Dong, Y. Sun, M. Fu, Z. Wu, S. C. Lee, Journal of Hazardous Materials **219-220**, 26 (2012).
[11] A. Umar, R. Ahmad, R. Kumar, A. Ibrahim Ahmed, S. Baskoutas, Journal of Alloys and Compounds **683**, 433 (2016).
[12] Y. Zheng, F. Duan, M. Q. Chen, Y. Xie, Journal of Molecular Catalysis A: Chemical **317**(1-2), 34 (2010).
[13] F. Dong, W. K. Ho, S. C. Lee, Z. B. Wu, M. Fu, S. C. Zou, Y. Huang, Journal of Materials Chemistry **21**(33), 12428 (2011).
[14] P. Madhusudan, J. Zhang, B. Cheng, G. Liu CrystEngComm **15**(2), 231 (2013).
[15] Y. H. Ao, L. Y. Xu, P. F. Wang, C. Wang, J., Hou J. Qian, Y. Li, Applied Surface Science **355**, 411 (2015).
[16] P. Ju, P. Wang, B. Li, H. Fan, S. Y. Ai, D. Zhang, Y. Wang, Chemical Engineering Journal **236**, 430 (2014).
[17] F. M. Zhao, L. Pan, S. W. Wang, Q. Y. Deng, J. J. Zou, L. Wang, X. W. Zhang, Applied Surface Science **317**, 833 (2014).
[18] L. Chen, R. Huang, S. F. Yin, S. L. Luo, C. T. Au, Chemical Engineering Journal **193-194**, 123 (2012).
[19] Y. Lu, K. Zhao, Y. H. Zhao, S. Y. Zhu, X. Yuan, M. X. Huo, Y. Zhang, Y. Qiu, Colloids and Surfaces A: Physicochem. Eng. Aspects **481**, 252 (2015).
[20] Y. Li, W. J. Wu, M. Z. Wu, P. Dai, L. L. Zhang, Z. Q. Sun, G. Li, X. S. Liu, X. S. Chen, X. W. Zheng, Materials Research Bulletin **55**, 121 (2014).
[21] H. W. Huang, Y. He, X. W. Li, M. Li, C., Zeng F. Dong, X. Du, T. R. Zhang, Y. H. Zhang Journal of Materials Chemistry A **3**(48), 24547 (2015).
[22] H. W. Huang, X. Han, X. W. Li, S. C. Wang, K. Chu Paul, Y. H. Zhang, ACS Applied Materials & Interfaces **7**(1), 482 (2015).
[23] H. F. Cheng, B. B. Huang, Y. Dai, X. Y. Qin, X. Y. Zhang, Langmuir **26**(9), 6618 (2010).
[24] E. P. Gao, W. Z. Wang, M. S. Shang, J. H. Xu, Physical Chemistry Chemical Physics **13**(7), 2887 (2011).